Journal of Catalysis 266 (2009) 331–342

Contents lists available at ScienceDirect

Journal of Catalysis

journal homepage: www.elsevier.com/locate/jcat

Dendrimer-mediated synthesis of subnanometer-sized Rh particles supported on ZrO_2

Attilio Siani [a], Oleg S. Alexeev [a], D. Samuel Deutsch [a], John R. Monnier [a], Paul T. Fanson [b], Hirohito Hirata [c], Shinichi Matsumoto [c], Christopher T. Williams [a], Michael D. Amiridis [a,*]

[a] Department of Chemical Engineering, University of South Carolina, Columbia, SC 29208, USA
[b] Toyota Motor Engineering and Manufacturing, Inc., Ann Arbor, MI 48105, USA
[c] Toyota Motor Corporation, Higashifuji Technical Center, Shizuoka 410-1193, Japan

ARTICLE INFO

Article history:
Received 14 July 2008
Revised 21 June 2009
Accepted 28 June 2009
Available online 29 July 2009

Keywords:
Rhodium
Nanoparticles
Dendrimers
EXAFS
Ethane hydrogenolysis

ABSTRACT

We have achieved the synthesis of ZrO_2-supported Rh particles with sub-nanometer dimensions and very narrow particle size distributions using G4OH-PAMAM dendrimers as templates. The different steps of this process were characterized by EXAFS and HRTEM measurements. The results indicate that partially hydrolyzed Rh^{3+} species in an aqueous solution can interact with amide/amine groups in the interior of G4OH dendrimers to form $(Rh^{3+})_x$-G4OH complexes. Rh_3 clusters were subsequently formed in the same solution following room temperature reduction of the $(Rh^{3+})_x$-G4OH complexes with $NaBH_4$. These Rh_3 clusters can be delivered intact on the surface of the ZrO_2 support. The formation of highly dispersed and nearly uniform Rh particles with sizes below 1 nm was observed following thermal removal of the dendrimer component. The structure-sensitive reaction of ethane hydrogenolysis was used for the evaluation of Rh/ZrO_2 samples with different metal particle sizes. A substantial decrease in turnover frequency was observed when the particle diameter decreased below 1.5 nm, consistent with mechanistic explanations advanced previously in the literature for this reaction.

1. Introduction

Supported mono- and bi-metallic catalysts are routinely used in large-scale catalytic processes, with examples including but not limited to automotive emission control, naphtha reforming, and direct methanol fuel cell applications [1–3]. In such catalysts the active metal component is typically dispersed over a high surface area support and its catalytic behavior can be affected by the size and shape of the metal nanoparticles formed, as well as their interactions with the support.

Catalysts incorporating supported metal nanoparticles with sizes below 1 nm have been classified in the past as an unexplored domain of catalytic materials, which are challenging to prepare and characterize [4]. More recent advances in the use of carbonyl or organometallic cluster precursors have allowed for the preparation of highly dispersed materials with nearly uniform sizes of metal clusters, and have shown – both experimentally and theoretically – that the physical and chemical properties of these materials can be substantially different from those of bulk metals [5–10]. Such properties can be induced by either geometric or electronic effects, both of which become more significant as the size of the metal particles becomes smaller. For example, sub-nanometer metal particles exhibit geometries in which the fraction of low coordination highly energetic (i.e., edges and corners), and therefore, reactive sites changes significantly with the dimension [11,12]. In addition, theoretical calculations show that many important parameters such as bond length, binding energy, stability function, fragmentation energy, bond dissociation energy, ionization potential, electron affinity, and dipole moment can fluctuate substantially with particle size [13]. Finally, just as ligands have an effect on the structure, electron distribution, and other electronic and magnetic properties of molecular clusters [14], the support may also be regarded as a ligand shell which is bonded to supported sub-nanometer metal particles. As a result, metal-support interactions are a crucial factor in altering the metallic character of the active sites in sub-nanometer supported metal particles, leading to unique catalytic properties [15]. Experimental results obtained for Pd, Ag, Cd, and Au particles of various sizes indeed show that such particles tend to become non-metallic in nature when their size decreases below 1 nm [16]. As a consequence, even traditional structure-insensitive reactions may also show signs of structure sensitivity in this domain [17].

While the use of organometallic and carbonyl cluster precursors offers better control over the metal dispersion [17,18], it suffers from difficulties associated with the handling of such precursors and the limited availability of appropriate clusters with a wide range of compositions. It has been also suggested that colloidal

* Corresponding author.
E-mail address: amiridis@engr.sc.edu (M.D. Amiridis).

0021-9517/$ - see front matter © 2009 Elsevier Inc. All rights reserved.
doi:10.1016/j.jcat.2009.06.025

nanoparticles preformed in solution can be used as precursors for the preparation of heterogeneous catalysts [19]. In this case, a precise tailoring of the size, shape, and composition of metal particles can be achieved in solution, thus eliminating high temperature post-treatments often used to create such metal particles during conventional catalyst preparations. The preparation of colloidal metal suspensions requires the chemical reduction of transition metal salts in an aqueous or organic medium in the presence of surfactants that act as protective agents in order to preserve the colloidal state of metal particles [20–22]. Several chemical compounds, such as poly(vinyl pyrrolidone) (PVP), poly(vinyl alcohol) (PVA), polyoxoanions, and other compounds containing amide and/or amine groups have been used in this role [20–22]. Interactions of these surface-active chemicals with metal particles are strong enough to limit the particle growth in solution, and therefore, nearly monodispersed metal nanoparticles, typically in the 1–3 nm size range, can be formed [23]. Literature reports demonstrate a successful grafting of colloidal metal nanoparticles onto various supports, and such catalysts typically show narrower particle size distributions than those observed with traditionally impregnated catalysts on similar supports with the same metal loading [19,24–27].

This report is focused on the use of PAMAM dendrimers as templates for the preparation of ZrO_2-supported Rh catalysts. PAMAM dendrimers offer a promising path to a rational design of nanostructured-supported metal catalysts because these hyperbranched polymers offer the ability to control the number of metal atoms complexed with their interior amide and amine functional groups, and therefore, in principle, the size of the metal particles eventually formed [28,29]. However, previous attempts to use this approach for the preparation of supported catalysts were not completely successful. For example, while it was shown that Pt-dendrimer nanocomposites contain very small Pt clusters in aqueous solutions, their deposition onto γ-Al_2O_3 leads to further nucleation and sintering of Pt, which is substantially accelerated during the removal of the dendrimer component [30]. Furthermore, the earlier mechanism used in the literature to describe the steps of this preparation route appears to represent only an ideal case and may not apply for all metals [28,29]. Recent data obtained using *in situ* EXAFS measurements suggest that the various preparation steps are more complex than originally anticipated and are likely to be dependent on the nature of the metal used [31]. For example, the addition of a reducing agent to metal-dendrimer complexes in solution can result in the formation of structures that retain certain valence characteristics of the metal precursor, instead of the formation of zerovalent nanoparticles [31]. The second major concern is the removal of the dendrimer shell and its decomposition products from the support, while limiting the sintering of the resulting supported metal nanoparticles. Even though it was shown that the size of metal particles in supported catalysts prepared via the dendrimer route can be controlled within a relatively narrow range [19,24–27], no catalysts with subnanometer-sized metal particles were prepared to date via this synthetic route, to the best of our knowledge.

In this report, we provide evidence for the successful preparation of nearly uniform, subnanometer-sized Rh particles via a dendrimer-mediated synthetic route on a ZrO_2 support. EXAFS spectroscopy was used to monitor the coordination environment of Rh throughout all preparation steps, and HRTEM measurements were used to image the resulting supported metal nanoparticles. Finally, their catalytic properties were probed via the structure-sensitive ethane hydrogenolysis reaction in an attempt to further confirm the presence of highly dispersed Rh nanoparticles via their catalytic behavior. These unique Rh/ZrO_2 materials could have potential applications in a large number of catalytic reactions.

2. Experimental

2.1. Reagents and materials

Fourth generation hydroxyl-terminated (G4OH) poly(amidoamine) (PAMAM) dendrimers were purchased as a 10% solution in methanol (Aldrich). Prior to use, the methanol was removed under N_2 flow at room temperature and a 0.17-mM aqueous solution of G4OH dendrimer was prepared. Milli-Q deionized water (18 MΩ cm) was used to prepare all aqueous solutions. Rhodium(III) chloride hydrate ($RhCl_3{\cdot}xH_2O$) (99.95% purity, Alfa Aesar) was used as supplied. A commercial powdered ZrO_2 support (Toyota Motor Engineering and Manufacturing North America) with a BET surface area of 45 m^2/g was calcined in air for 4 h at 500 °C prior to use. UHP grade H_2 and N_2 (National Welders) were additionally purified from traces of moisture and oxygen by passage through appropriate traps (Agilent, models GMT-2GCHP and OT-3, respectively), prior to use.

2.2. Preparation of Rh-dendrimer nanocomposites

Appropriate amounts of a 25.6-mM aqueous solution of $RhCl_3$ were added under nitrogen flow to a 0.17-mM aqueous solution of G4OH dendrimer in order to obtain Rh-G4OH nanocomposites with the desired Rh/dendrimer ratios. In each case, the mixture was stirred under nitrogen flow for 3 days to allow the complexation of Rh^{3+} cations with the amide/amine groups of the dendrimer. The complexes formed during this preparation step are denoted as $(Rh^{3+})_x$-G4OH, where x is the Rh/dendrimer molar ratio. After the complexation was completed, the solution was dialyzed to remove impurities using a benzoylated cellulose dialysis sack having a molecular weight cutoff of 2000. The resulting solutions were subsequently treated at room temperature under vigorous stirring with freshly prepared aqueous solutions of sodium borohydride ($NaBH_4$). In each case, the $NaBH_4$/Rh weight ratio was fixed to 8. Such a treatment resulted in the formation of Rh-dendrimer nanocomposites denoted as Rh_x-G4OH, where x is the Rh/dendrimer molar ratio.

2.3. Preparation of supported samples

Supported samples were prepared by slurrying a Rh_x-G4OH solution with the ZrO_2 support in amounts chosen to yield a Rh loading of approximately 1.0 wt.%. The excess water was removed by slow evaporation at room temperature, followed by evacuation. The resulting solid samples were treated in an O_2/He mixture at 425 °C for 1 h followed by H_2 at 300 °C for 1 h to remove the dendrimer component and reduce the remaining Rh particles to the metallic state. Reference samples containing 1, 2, and 5 wt.% Rh were synthesized via standard incipient wetness impregnation using the same $RhCl_3{\cdot}xH_2O$ precursor and treated under conditions identical to those used for the dendrimer-derived samples. The Rh weight loading was verified in each sample by inductively coupled plasma-mass spectroscopy (ICP-MS) analysis (Galbraith Laboratories Inc.).

2.4. HRTEM measurements

HRTEM images were obtained at Oak Ridge National Laboratory with a Hitachi HF-2000 instrument equipped with a cold field emission electron source operating at 200 keV. Each solid sample was finely crushed before deposition on a carbon-coated Cu grid. All images were acquired digitally and processed by a Gatan imaging filter. The point-to-point resolution was 0.24 nm. Surface-averaged sizes of the metal particles were calculated as reported

elsewhere [32] using at least 200 particles from at least 5 different micrographs for each sample.

2.5. EXAFS spectroscopy

EXAFS spectra were collected at X-ray beamline 2–3 at the Stanford Synchrotron Radiation Laboratory (SSRL), Stanford Linear Accelerator Center, Menlo Park, CA. The storage ring electron energy was 3 GeV and the ring current was in the range of 80–100 mA.

The EXAFS data for aqueous solutions and solid samples were recorded at room temperature in the fluorescence mode with a 13-element Ge array detector. Liquid and solid samples were loaded into *in situ* EXAFS cells designed to allow handling of samples without air exposure. The total count rate for the 13-element Ge array detector was in the range of 30,000–40,000 counts per second. It has been experimentally established that the detector readings are linear within this range and no corrections for deadtime are required. Samples were scanned at the Rh *K* edge (23220 eV). Data were collected with a Si(220) double crystal monochromator that was detuned by 30% to minimize the effects of higher harmonics in the X-ray beam. Raw EXAFS functions for all samples examined are shown in Fig. 1.

2.6. EXAFS data analysis

The EXAFS data at the Rh *K* edge were analyzed with experimentally determined reference files obtained from EXAFS data characterizing materials of known structure. The Rh–Rh (for the first and the second shells), Rh–N(O), Rh–Cl, and Rh^{3+}–Rh^{3+} contributions were analyzed with phase shifts and backscattering amplitudes obtained from EXAFS data characterizing Rh foil, Rh_2O_3, and anhydrous $RhCl_3$, respectively. The crystallographic coordination parameters for all reference compounds, the weighting of the Fourier transform, and the ranges in *k* and *r* space used to extract the reference functions from the experimental EXAFS data are reported elsewhere [33]. The EXAFS parameters were extracted from the raw data with the aid of the XDAP software [34] using methods that are essentially the same as those reported elsewhere [35]. The raw EXAFS data obtained were analyzed over the ranges of *k* (the wave vector) and *r* (the distance from the absorbing Rh atom) that are specified for each sample in Table 1, with a maximum number of free parameters not exceeding the statistically justified value estimated on the basis of the Nyquist theorem [36,37]. The data used for each sample were the averages of six scans. The parameters characterizing both the high-Z (Rh–Rh, Rh^{3+}–Rh^{3+}) and low-Z (Rh–$O_{support}$, Rh–Cl, Rh–N(O)) contributions for the samples examined were determined by multiple-shell fitting in *r*-space with application of k^1 and k^3 weighting in the Fourier transformations [35,38]. The fit was optimized by use of a difference file technique with phase- and amplitude-corrected Fourier transforms of the data [38–40].

Standard deviations for the various parameters were calculated from the covariance matrix, taking into account the statistical noise of the EXAFS data and the correlations between the different coordination parameters as described elsewhere [41]. The values of the goodness of fit (ε_ν^2) were calculated as outlined in the Reports on Standards and Criteria in XAFS Spectroscopy [42]. The variances in both the imaginary and absolute parts were used to determine the quality of the fit [43].

2.7. Hydrogen chemisorption and temperature programmed oxidation

Rhodium dispersions and surface site concentrations were estimated using a Micromeritics 2920 AutoChem II pulse chemisorption analyzer. Prior to chemisorption, catalysts were reduced in flowing H_2 at 300 °C for 1 h, and then flushed with Ar for 1 h at 300 °C before cooling down to 40 °C in Ar. Each sample was then exposed to 10% O_2/He mixture for 30 min, flushed with Ar for 30 min, and finally analyzed by pulsed H_2 titration of the oxygen pre-covered Rh sites. The stoichiometry of this H_2 titration was assumed to be one Rh site for every 3/2 H_2 molecules consumed, as previously used by Boudart et al. [44]. Rh dispersion values were calculated based on the number of surface Rh sites thus titrated and the total Rh loading.

Temperature programmed oxidation (TPO) measurements were conducted using approximately 50 mg of powdered sample loaded into a quartz tubular reactor placed in a split tube furnace and heated at linear rates up to 50 °C/min. Sample temperatures were measured by a thermocouple embedded in the catalyst bed. All gases were supplied by National Welders and passed through H_2O and/or O_2 traps (Restek). Gas flow rates were controlled by mass flow controllers, while an MDC variable leak valve was used to adjust gas leak rates into an Inficon Transpector 2 residual gas analyzer (RGA). Sample temperatures and mass intensity data for the gases of interest were collected and stored in a dedicated computer using TWare32 Single Sensor software. Before TPO analysis, all samples were pretreated in 20 standard ml/min of flowing He as the temperature was ramped at 10 °C/min to 570 °C to remove residual and chemisorbed H_2O and CO_2 from the samples. After cooling the samples to 30 °C in flowing He, the gas flow was changed to the 10% O_2/He mixture (20 standard ml/min total flow) and the temperature was ramped at 10 °C/min to a final temperature of 570 °C. Mass intensity data for H_2O^+, CO^+, NO^+, CO_2^+, and NO_2^+ were routinely monitored and stored for each sample.

2.8. Ethane hydrogenolysis

Ethane hydrogenolysis measurements were conducted in a 0.25-in. diameter stainless steel fixed-bed flow reactor. The flow rates of hydrogen (99.999%), ethane (99%), and helium (99.999%) were controlled by mass flow controllers to achieve a reacting mixture with the following composition: 20% H_2, 5% C_2H_6, and 75% He. A total volumetric flow rate of 200 standard ml/min for a catalyst mass of 0.1 g was used for each experiment. The reaction feed and product streams were analyzed using an on-line GC (HP 5890) equipped with dual 30 m Poraplot Q capillary columns. Both TCD and FID detectors were used for quantitative analysis of the reaction feed and products. The reaction was conducted at differential conditions in the 150–220 °C temperature range. Since deactivation of catalysts may take place at non-negligible rates due to the buildup of carbon on the catalyst surface [45], ethane was added to the hydrogen/helium feed stream for only 5 min intervals at a chosen temperature before the analysis of products was made. The flow of ethane was diverted after each injection, while the hydrogen/helium mixture continued to flow over the catalyst bed. Furthermore, when the catalyst evaluation was completed, each sample was tested again at the initial conditions (i.e., temperature and feed composition) to confirm that deactivation had not occurred.

3. Results and discussion

EXAFS spectroscopy was used to obtain structural information characterizing the local environment of the Rh atoms throughout each step involved in the synthesis of the dendrimer-derived Rh/ZrO_2 catalysts. Such an approach allowed us to reach a better molecular-level understanding of the processes taking place during the synthesis. The structural parameters determined for various samples are summarized in Table 1, and comparisons of the raw data and fits in *r* space are shown in Fig. 2.

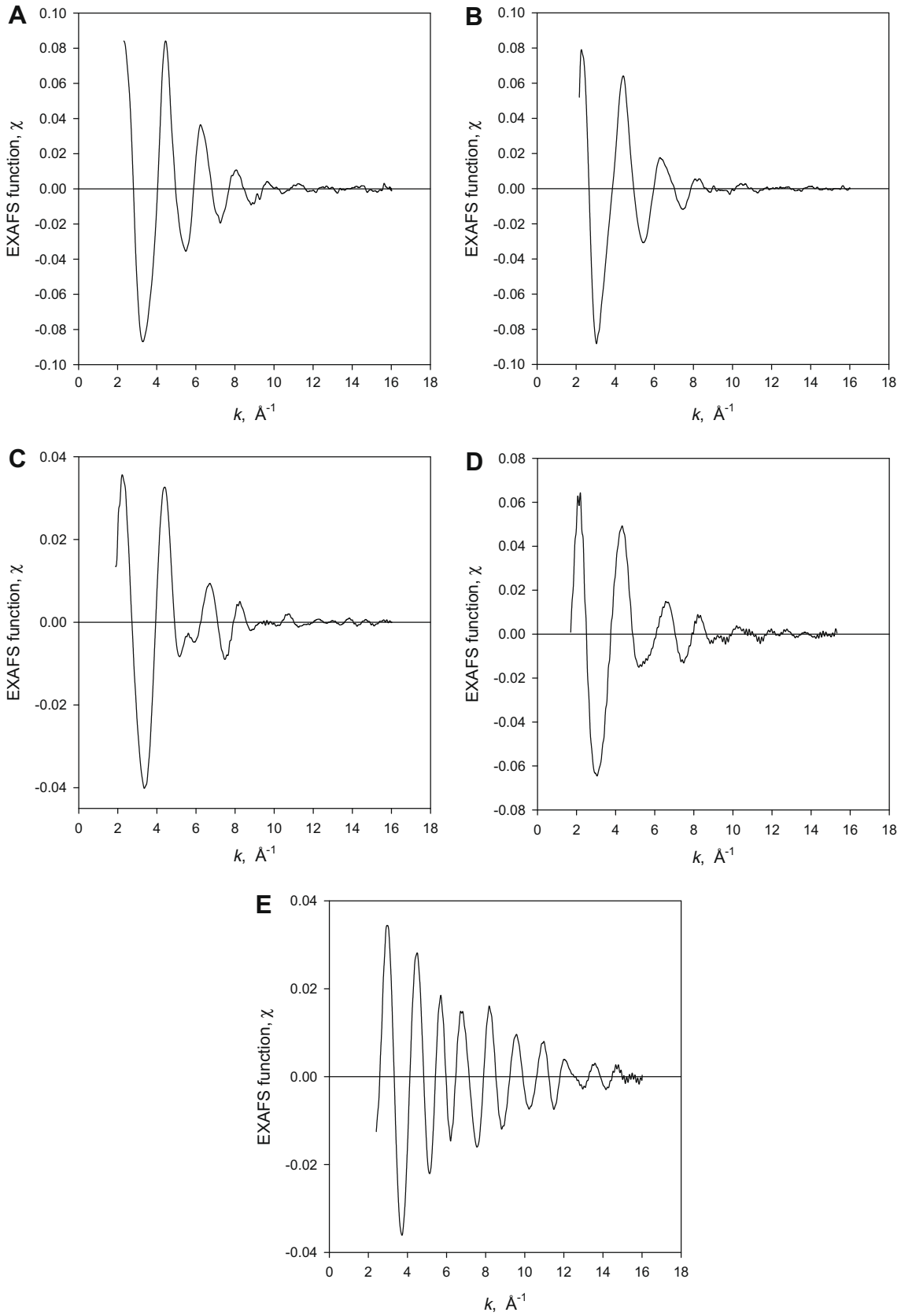

Fig. 1. Raw EXAFS functions of (A) $RhCl_3$ in aqueous solution, (B) $(Rh^{3+})_{20}$-G4OH in aqueous solution, (C) ($Rh^{3+})_{20}$-G4OH treated with $NaBH_4$ in aqueous solution, (D) Rh_{20}-G4OH/ZrO_2 as prepared, and (E) Rh_{20}-G4OH/ZrO_2 following treatments with O_2 at 425 °C and H_2 at 300 °C.

Table 1
Structural parameters characterizing the species formed at various steps involved in the preparation of dendrimer-derived Rh/ZrO_2 catalysts.

Sample	Shell	N	$\Delta\sigma^2$ (Å^2)	R (Å)	ΔE_0 (eV)	ε_ν^2	k^1-Variances (%)	
							abs	im
$RhCl_3/H_2O$[a]	Rh^{3+}–Rh^{3+}	–	–	–	–	1.8	0.7	0.5
	Rh–O	3.2	0.00045	2.09	−5.5			
	Rh–Cl	3.0	−0.00022	2.30	−0.5			
$(Rh^{3+})_{20}$-G4OH[a]	Rh^{3+}–Rh^{3+}	0.9	0.00184	3.03	9.0	2.7	0.3	1.0
	Rh–N(O)	4.0	0.00275	2.05	0.2			
	Rh–Cl	1.5	0.00212	2.30	0.6			
$(Rh^{3+})_{20}$-G4OH[a] treated with $NaBH_4$ in aqueous solution	Rh–Rh	2.2	0.00988	2.69	3.3	1.9	0.3	0.8
	Rh–N(O)	2.7	0.00554	2.05	0.7			
	Rh–Cl	–	–	–	–			
Rh_{20}-G4OH/ZrO_2[a] as prepared	Rh–Rh	2.0	0.01000	2.69	2.7	2.0	1.0	2.4
	Rh–$N(O)_1$	4.4	0.00284	2.05	4.4			
	Rh–$N(O)_2$	0.3	−0.00493	2.42	7.5			
Rh_{20}-G4OH/ZrO_2[b] treated with O_2 at 425 °C and H_2 at 300 °C	Rh–Rh_1	4.6	0.00502	2.68	2.2	1.6	0.5	0.8
	Rh–Rh_2	1.2	0.00144	3.80	0.1			
	Rh–$O_{support}$							
	Rh–O_s[c]	1.4	0.00274	2.15	−9.7			
	Rh–O_l[c]	0.9	0.00045	2.35	1.5			

Standard deviations in fits: $N \pm 20\%$, $R \pm 1\%$, $\Delta\sigma^2 \pm 5\%$, $\Delta E_0 \pm 10\%$. N: coordination number; R: distance between absorber and backscatterer atoms; $\Delta\sigma^2$: difference in the Debye-Waller factor between the sample and the reference compound; ΔE_0: difference in the inner potential between the sample and the reference compound; ε_ν^2: goodness of fit.

[a] Fit ranges $3.50 < k < 15.00$ Å^{-1} and $1.0 < r < 3.0$ Å, number of allowed fitting parameters 15.

[b] Fit ranges $3.50 < k < 15.00$ Å^{-1} and $1.0 < r < 3.5$ Å, number of allowed fitting parameters 19.

[c] The subscripts s and l refer to short and long, respectively.

3.1. Synthesis of Rh-dendrimer nanocomposites in solution

The solid $RhCl_3$ precursor used consists of polynuclear species with a pseudo-hexagonal layer lattice structure, in which each Rh^{3+} cation is surrounded by 6 chlorine atoms; the average distance between Rh^{3+} cations is 3.43 Å [46,47]. The EXAFS data reported in Table 1 for an aqueous solution containing 250 ppm of $RhCl_3$ indicate that the first coordination shell of the Rh^{3+} cations consists on average of 3.0 chlorine and 3.2 oxygen atoms at Rh–Cl and Rh–O bonding distances of 2.30 and 2.09 Å, respectively. The observed Rh–O contributions represent aquo ligands (i.e., H_2O), while the presence of only 3.0 chlorine atoms in the first coordination shell of Rh and the complete absence of Rh^{3+}–Rh^{3+} contributions indicate that the polynuclear $RhCl_3$ species are converted to monomers in solution. Furthermore, the sum of nearest neighbors in the first coordination shell of Rh is approximately 6, suggesting that the Rh^{3+} cations remain in an octahedral environment. Hydrated $[RhCl_3(H_2O)_3]$ complexes appear to be the primary species formed in the aqueous solution, in agreement with earlier literature reports postulating the formation of such neutral complexes based on UV–VIS and NMR data [48–50].

When the aqueous solution containing the $[RhCl_3(H_2O)_3]$ species is further brought in contact with the G4OH PAMAM dendrimer, complexation of Rh^{3+} with the nitrogen moieties of the dendrimer is expected to take place, similar to what was described previously for Pt^{4+} and Pt^{2+} cations [30]. A direct distinction between oxygen and nitrogen neighbors is problematic from the EXAFS data, since these two elements are neighbors in the periodic table and have similar phase shifts and backscattering amplitudes. It is generally assumed that the phase shifts and backscattering amplitudes are transferable among nearest neighbors in the periodic table [51]. Consequently, we have been analyzing Rh–N and Rh–O contributions as a group (denoted as Rh–N(O)), without distinguishing between the oxygen and nitrogen backscatterers. The EXAFS data summarized in Table 1 show that the interaction of an aqueous solution of $[RhCl_3(H_2O)_3]$ with the dendrimer leads to a decrease in Rh–Cl contributions and a simultaneous increase in Rh–N(O) contributions. More specifically, the first coordination shell of Rh in $(Rh^{3+})_{20}$-G4OH consists on average of approximately 1.5 chlorine atoms at a bond distance of 2.30 Å and 4.0 oxygen/nitrogen atoms at a bond distance of 2.05 Å. The increase of N(O) neighbors is indicative of the interactions between Rh^{3+} cations and the dendrimer's nitrogen-containing amide and tertiary amine groups. These functional groups are more basic than aquo ligands and are capable of participating in the observed displacement of chlorine atoms from the first coordination shell of Rh, probably via a nucleophilic attack on the Rh^{3+} cations. Since the band structure in the Rh K-edge XANES region is nearly the same as that of the precursor (Fig. 3), we can infer that the electronic state of Rh remains unchanged after interactions with the dendrimer. Once again, the total sum of nearest neighbors in the first coordination shell of Rh remains approximately 6, indicating that Rh^{3+} cations maintain an octahedral geometry even after the interaction with the dendrimer.

High-Z backscatterers were also present in the second coordination shell of Rh. In particular, Rh^{3+}–Rh^{3+} interactions were identified with an average coordination number of 0.9 at a distance of 3.03 Å (Table 1). This distance is too long to be a bonding distance and is substantially different from that (i.e., 3.43 Å) observed for Rh^{3+}–Rh^{3+} pairs in the solid $RhCl_3$ precursor [33]. Therefore, these contributions may represent neighboring Rh^{3+} cations complexed with adjacent functional groups in the dendrimer interior.

When an aqueous solution of $(Rh^{3+})_{20}$-G4OH was subsequently treated with $NaBH_4$, the analysis of the EXAFS spectra indicates the presence of Rh–Rh contributions with an average coordination number of 2.2 at a bond distance of 2.69 Å (Table 1). Since higher Rh–Rh shells were not observed in the spectra, this result suggests the formation of isolated Rh clusters incorporating on average approximately three Rh atoms. Evidently, the reduction treatment with $NaBH_4$ also helps to remove the remaining Cl ligands, since no Rh–Cl contributions were any longer present in the spectra. The prevailing theory regarding metal cation interactions with dendrimers [28,29] suggests that at the completion of the reduction treatment, zerovalent dendrimer-stabilized metal nanoparticles should be formed with sizes corresponding to the number of metal atoms initially complexed within each single dendrimer macro-

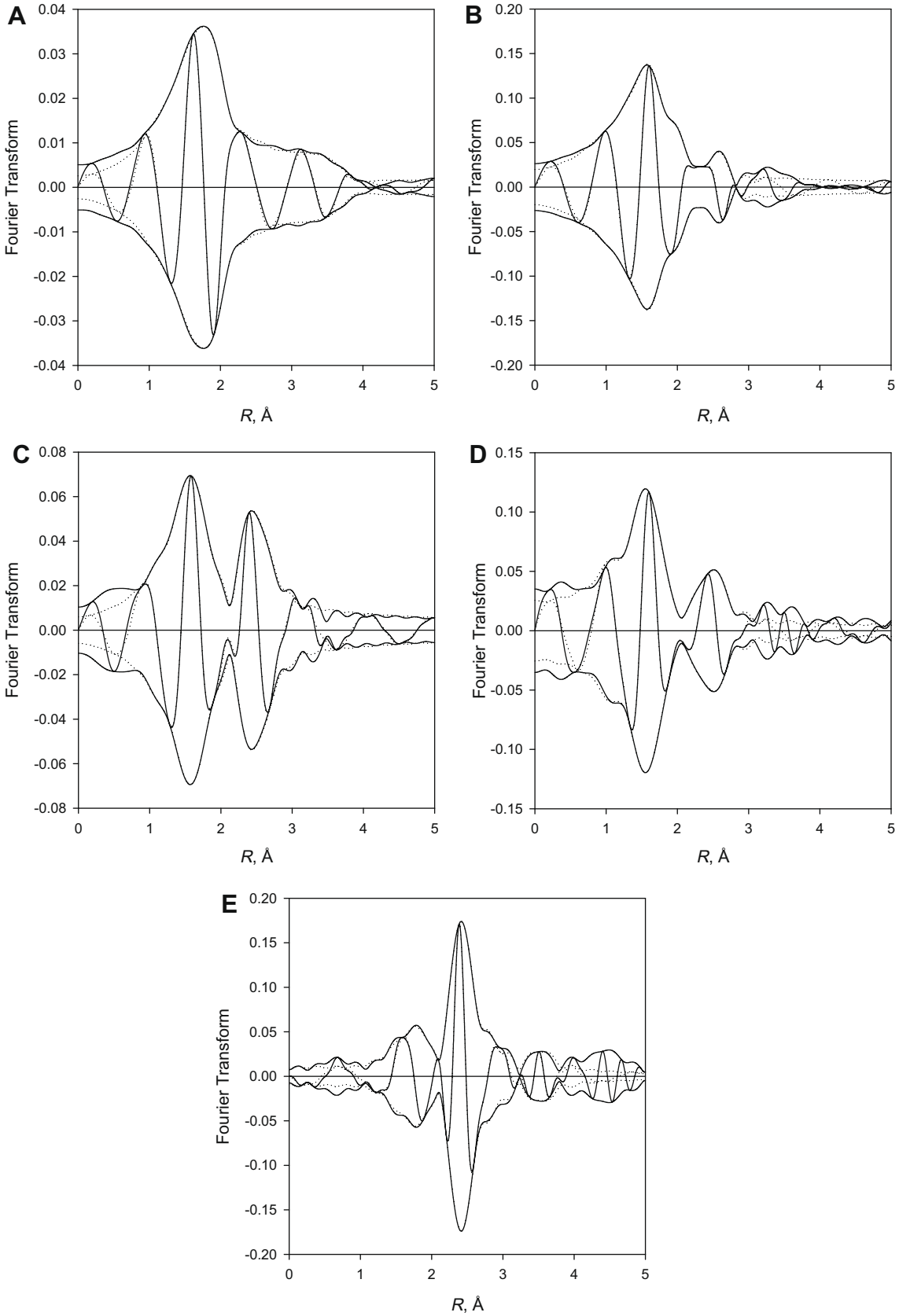

Fig. 2. EXAFS spectra collected at the Rh *K* edge and corresponding fits for (A) $RhCl_3$ in aqueous solution; (B) $(Rh^{3+})_{20}$-G4OH in aqueous solution; (C) $(Rh^{3+})_{20}$-G4OH treated with $NaBH_4$ in aqueous solution; (D) Rh_{20}-G4OH/ZrO_2 as prepared; (E) Rh_{20}-G4OH/ZrO_2 following treatments with O_2 at 425 °C and H_2 at 300 °C. Imaginary part and magnitude of uncorrected Fourier transform (k^1-weighted) of experimental EXAFS shown as solid lines, while sum of the calculated contributions as stated in Table 1 is shown as dotted lines.

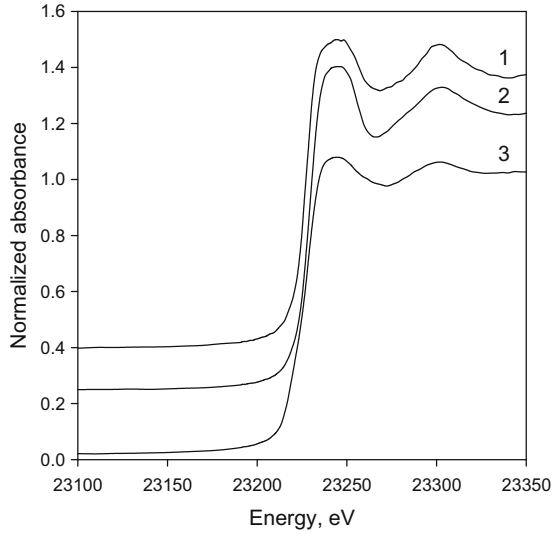

Fig. 3. XANES spectra of (1) $RhCl_3$ in aqueous solution, (2) $(Rh^{3+})_{20}$-G4OH in aqueous solution, and (3) $(Rh^{3+})_{20}$-G4OH treated with $NaBH_4$ in aqueous solution.

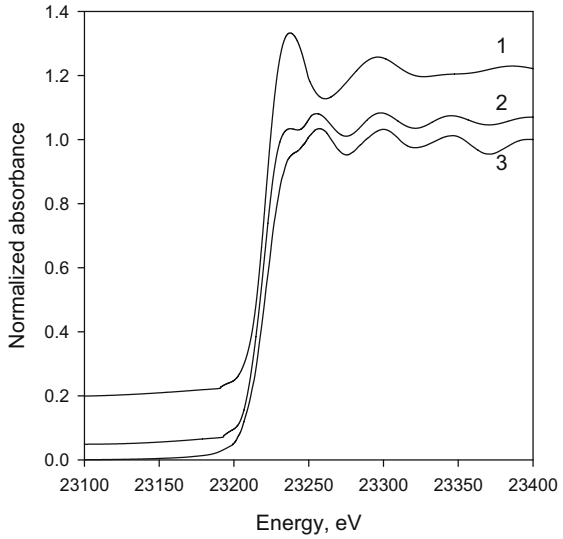

Fig. 4. XANES spectra of (1) Rh_{20}-G4OH/ZrO_2 as prepared, (2) Rh_{20}-G4OH/ZrO_2 following treatments with O_2 at 425 °C and H_2 at 300 °C, and (3) Rh foil.

molecule. In contrast, our EXAFS data clearly indicate that the Rh atoms remained highly dispersed within the dendrimer structure, and only small Rh_3 clusters were formed. Moreover, the Rh *K*-edge XANES data shown in Fig. 3 (spectrum 3) indicate that the white line area decreased only slightly after the treatment with $NaBH_4$, suggesting that the clusters formed incorporate Rh in a cationic form. Similar results were also reported for $(Pt^{4+})_{40}$-G4OH nanocomposites in aqueous solutions [30]. The Rh_3 clusters formed remained strongly bonded to the dendrimer, as evidenced by the presence of substantial Rh–N(O) contributions with an average coordination number of 2.7 at a bond distance of 2.05 Å (Table 1). The presence and strength of such bonding may explain the high dispersion of Rh within the dendrimer structure that prevents the formation of larger metallic nanoparticles.

3.2. Impregnation on the support

Following impregnation of the $NaBH_4$-treated Rh_{20}-G4OH aqueous solution onto the ZrO_2 support and subsequent drying and evacuation at room temperature, the analysis of the EXAFS spectra suggests the presence of Rh–Rh contributions with an average coordination number of approximately 2.0 at a bond distance of 2.69 Å (Table 1). Since the average Rh–Rh coordination number and the Rh–Rh bond distance are approximately the same as those observed for the Rh_3 clusters formed in solution, we infer that the structure of the Rh_3 clusters remains intact following the impregnation on the ZrO_2 support. Once again, the Rh *K*-edge XANES band structure (Fig. 4, spectrum 1) resembles that of $(Rh^{3+})_{20}$-G4OH in aqueous solution, indicating that Rh still remains in a cationic form after the impregnation step.

The EXAFS data further indicate that these ZrO_2-supported Rh_3 clusters remain in close contact with the dendrimer, as evidenced by the presence of a substantial number of N(O) backscatterers (Table 1). In this case, approximately 4.4 N(O) first-shell neighbors were observed at an average distance of 2.05 Å, along with approximately 0.3 N(O) backscatterers located at a longer distance of 2.42 Å. Therefore, the total number of N(O) atoms surrounding the Rh_3 clusters in the supported species is approximately 4.7, which is somewhat larger than that observed for Rh_3 clusters in solution (Table 1). This observed increase of N(O) backscatterers in the neighborhood of Rh is probably related to changes in the structure of the dendrimer. PAMAM dendrimers in solution have an open, nearly spherical, shaped structure [52]. However, in the absence of a solvent, PAMAM dendrimers deposited on a solid support lose a substantial portion of their volume, resulting in the collapse of the dendrimer's branches [53,54]. It is likely that upon such a configurational dendrimer collapse, Rh_3 clusters entrapped in the dendrimer also come to closer contact with the branches of the dendrimer, resulting in the observed increase in the average number of N(O) neighbors. However, we cannot exclude the possibility that some Rh_3 clusters also become exposed to the support surface, which could lead to an increase in the Rh–N(O) coordination number as well.

3.3. Removal of the dendrimer component

It has been shown previously that supported metal-dendrimer nanocomposites have the ability to catalyze reactions in the liquid phase [19]. However, when the solvent is removed, the metal sites are no longer accessible even to small gaseous molecules due to interference from the collapsed dendrimer [24,54–56]. Therefore, the dendrimer removal is an important step in the activation of solid catalysts prepared via this synthetic route. Optimal conditions for the removal of the dendrimer shell were established based on FTIR measurements conducted on Rh_{20}-G4OH/ZrO_2 catalysts and reported separately [57]. The FTIR results suggest that, under oxidizing conditions, partial decomposition of the dendrimer starts at a temperature as low as 50 °C and is completed at approximately 200 °C. However, various carboxylate species, which are formed on the catalyst surface as a result of the dendrimer decomposition, undergo further transformations and the decomposition fragments formed continue to impede the accessibility of the Rh sites following treatment temperatures of up to 300 °C. Finally, a completely clean catalyst surface can be obtained during FTIR measurements after oxidation of the sample at 425 °C for 1 h.

To further investigate the dendrimer removal and to address concerns regarding the possible effects of residual carbon-containing species on the catalytic performance of the dendrimer-derived catalysts, TPO and carbon elemental analysis measurements were conducted before and after treatment in O_2/He at 425 °C. A non-Rh-containing G4OH/ZrO_2 sample, as well as Rh_{10}-G4OH/ZrO_2 and Rh_{20}-G4OH/ZrO_2 samples, were used in this process. While substantial carbon amounts (of the order of 3–5 wt.% depending on the dendrimer loading used during preparation) were detected

by elemental analysis on the non-treated samples, the carbon content for all samples treated in O_2/He at 425 °C was below the detection limit (0.1%). Furthermore, the TPO measurements conducted with the G4OH/ZrO_2 and Rh_{20}-G4OH/ZrO_2 samples yielded total amounts of CO_2 formed corresponding to 0.08 and 0.01 wt.% carbon, respectively. These results are consistent with our previous FTIR observations and indicate that Rh facilitates to some degree the dendrimer decomposition. A second successive TPO measurement in the case of the Rh_{20}-G4OH/ZrO_2 sample yielded no additional CO_2 formed. Overall, these results suggest that the oxidation treatment applied is sufficient to remove the majority of the carbon residues from the catalyst surface. In fact, even if all the remaining 0.01 wt.% carbon in the case of the Rh_{20}-G4OH/ZrO_2 sample was associated with Rh sites (which is highly unlikely) only 10% of the Rh sites would be covered by carbon.

It is expected that the treatment of the sample in O_2 at 425 °C will also lead to the fragmentation of Rh_3 clusters, resulting in the formation of site-isolated Rh oxide-type species. However, the EXAFS data show that a subsequent treatment of oxidized Rh_{20}-G4OH/ZrO_2 in H_2 at 300 °C for 1 h leads to the reappearance of Rh–Rh contributions at a bond distance of 2.68 Å (Table 1). In addition, short and long Rh–$O_{support}$ contributions are detected, with average coordination numbers of 1.4 and 0.9 at bond distances of 2.15 and 2.35 Å, respectively, signifying interactions of the Rh nanoparticles formed with the support. The Rh *K*-edge XANES spectrum characterizing this sample (Fig. 4, spectrum 2) no longer resembles that of Rh^{3+} cations but is similar to the spectrum of Rh foil, indicating that the thermal treatment leads to a complete reduction of Rh cations. The differences in the white line intensities observed for the ZrO_2-supported sample and Rh foil (Fig. 4) suggest that the ZrO_2-supported Rh nanoparticles formed are more electron deficient than bulk Rh, consistent with previous literature reports [58].

It was demonstrated previously that nearly uniform MgO-supported Rh_6 clusters can be completely fragmented in O_2 at 200 °C and then reconstructed by treatment in H_2 at approximately 300 °C [59]. However, the reconstruction of the Rh_6 octahedra was accompanied by some migration and aggregation of these clusters [60]. In our case, exact reconstruction of the Rh_3 clusters did not take place, as evidenced by the increase of the Rh–Rh first-shell contributions to approximately 4.6, and the appearance of second-shell Rh–Rh contributions with a coordination number of 1.2 at a distance of 3.80 Å (Table 1). These data clearly indicate that some aggregation of Rh took place during the removal of the dendrimer shell. However, the degree of such aggregation was obviously very small and the Rh nanoparticles finally formed on the ZrO_2 surface are highly dispersed. Known relationships between the average size of metal particles and the first-shell metal–metal coordination numbers reported by Kip et al. [61] indicate that the coordination number of 4.6 determined for the first-shell Rh–Rh contributions corresponds to Rh nanoparticles with an average diameter of approximately 8.5 Å. Such Rh nanoparticles incorporate no more than 20 metal atoms, with nearly 100% of these atoms exposed on the surface [61]. This size is similar to the Rh loading in each individual dendrimer structure. Thus, it is possible that only the Rh clusters within the vicinity of each single dendrimer molecule agglomerated to produce each Rh nanoparticle. Results obtained with materials produced with different Rh/dendrimer ratios (Table 2) are consistent with such a hypothesis and demonstrate that at least in the case of Rh/ZrO_2, precise control of the metal nanoparticles size can be achieved in these dendrimer-derived catalysts.

HRTEM images obtained for the Rh_{10}-, Rh_{20}-, and Rh_{40}-G4OH/ZrO_2 samples confirmed the presence of highly dispersed Rh particles in all cases. An example of such an image of the Rh_{20}-G4OH/ZrO_2 sample is shown in Fig. 5, while particle size distributions obtained for all samples are shown in Fig. 6. The dendrimer-derived Rh_{10}-G4OH/ZrO_2 and Rh_{20}-G4OH/ZrO_2 samples exhibited surface-averaged metal particle sizes of 0.7 and 0.8 nm, respectively. Furthermore, the distributions observed in these cases were very narrow and all particles were within the 0.4–1.4 nm range. Based on Rh lattice parameter calculations, semi-spherical rhodium particles consisting of 10 and 20 atoms are estimated to exhibit diameters of approximately 0.6 and 0.8 nm, respectively, consistent with what was observed experimentally. In contrast, a Rh/ZrO_2 sample prepared conventionally by incipient wetness impregnation and treated under identical conditions exhibited an average Rh particle diameter of 1.6 nm, corresponding to approximately

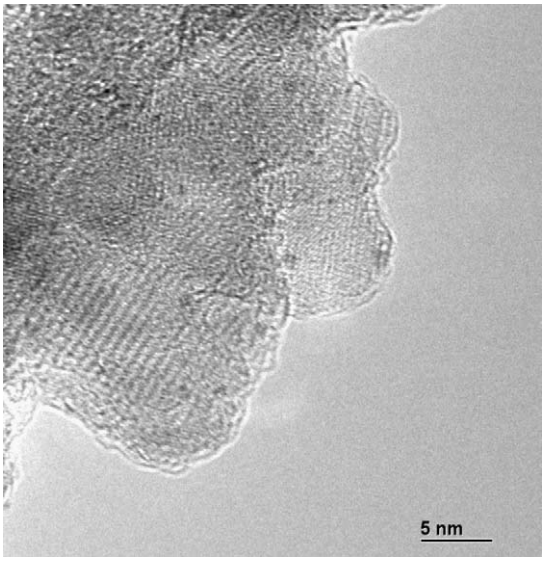

Fig. 5. HRTEM image of the Rh_{20}-G4OH/ZrO_2 catalyst following treatments with O_2 at 425 °C and H_2 at 300 °C.

Table 2
Kinetic results for ethane hydrogenolysis catalyzed by ZrO_2-supported rhodium catalysts (Reaction feed: 5% C_2H_6, 20% H_2, 75% He).

Sample	H/Rh	Average Rh particle size (nm)	Rh dispersion	E_a[a] (kcal/mol)	TOF at 200 °C[a] (min^{-1})
5 wt.% Rh/ZrO_2 incipient wetness	0.18	6.0[b]	0.19	39	3.6
2 wt.% Rh/ZrO_2 incipient wetness	0.55	2.0[b]	0.57	37	3.7
1 wt.% Rh/ZrO_2 incipient wetness	0.58	1.5[c]–1.9[b]	0.60	38	5.7
1 wt.% Rh_{40}-G4OH/ZrO_2	–	1.3[c]	0.82	43	0.096
1 wt.% Rh_{20}-G4OH/ZrO_2	0.11	0.8[c]	1.0	29	0.0043
1 wt.% Rh_{10}-G4OH/ZrO_2	0.10	0.7[c]	1.0	28	0.0016

[a] E_a, apparent activation energy; TOF, turnover frequency.
[b] Average particle size determined by H_2 chemisorption.
[c] Average particle size measured by TEM.

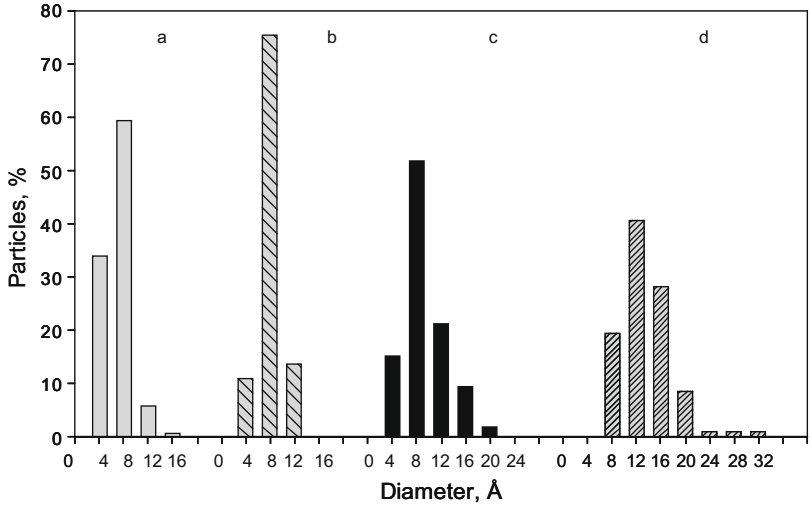

Fig. 6. Particle size distributions characterizing 1 wt.% (a) Rh_{10}-G4OH/ZrO_2, (b) Rh_{20}-G4OH/ZrO_2, (c) Rh_{40}-G4OH/ZrO_2, and (d) Rh/ZrO_2 (prepared via incipient wetness impregnation) treated with O_2 at 425 °C and H_2 at 200 °C.

150 Rh atoms. The particle size distribution in this case included particles ranging in size between 0.6 and 3.2 nm.

3.4. Hydrogen chemisorption and Rh dispersion

H/Rh values determined by pulsed H_2 titration of oxygen preadsorbed on Rh sites are shown in Table 2. The average size of Rh particles estimated from these measurements for the 1 wt.% Rh/ZrO_2 sample prepared by incipient wetness impregnation (i.e., 1.9 nm) agrees well with that determined from HRTEM (i.e., 1.5 nm), indicating that both techniques provide reliable estimates of Rh particle sizes for this sample. However, this is not the case for the dendrimer-derived Rh_x-G4OH/ZrO_2 samples. According to the HRTEM data the average Rh particle sizes in the dendrimer-derived Rh_{10}-G4OH/ZrO_2 and Rh_{20}-G4OH/ZrO_2 samples are 0.7 and 0.8 nm, respectively. The EXAFS data reported in Table 1 for the same Rh_{20}-G4OH/ZrO_2 sample indicate the presence of Rh–Rh first-shell contributions with an average coordination number of 4.6 after removal of the dendrimer shell, corresponding to an average Rh particle size of 0.85 nm. Therefore, both the EXAFS and HRTEM results indicate the formation of subnanometer-sized Rh particles in these dendrimer-derived samples. Such small Rh nanoparticles are expected to have nearly 100% of the Rh atoms exposed on the surface. In contrast to this expectation, the H/Rh values characterizing both Rh_{10}-G4OH/ZrO_2 and Rh_{20}-G4OH/ZrO_2 samples were found to be of the order of 0.11, suggesting that the Rh particles in these samples could be as large as 10 nm.

Such a discrepancy between chemisorption and EXAFS/HRTEM data for the dendrimer-derived samples suggests that the chemisorptive properties of the subnanometer Rh particles formed in these samples are altered substantially. FTIR, TPO, and elemental analysis results described in a previous section indicate that if there is any residual carbon in these samples, its concentration is too small to cover any significant fraction of exposed Rh sites, and therefore, other factors must be accounted for.

The ZrO_2 support belongs to a family of reducible supports capable of exhibiting strong metal-support interactions (SMSI) [62,63]. As has been shown previously, various noble metals on such supports lose their ability for irreversible chemisorption of hydrogen following reduction treatments at temperatures above 500 °C [62,63]. More recent literature reports summarizing data obtained for various model catalysts by X-ray photoelectron spectroscopy and low-energy ion scattering suggest that these SMSI effects can be observed even at reduction temperatures as low as 170 °C [64,65]. The nature of this phenomenon was described in detail in several publications [66]. For supported metal particles smaller than 1 nm in diameter (such as the ones observed in the case of the dendrimer-derived Rh_{10}-G4OH/ZrO_2 and Rh_{20}-G4OH/ZrO_2 samples), the metal-support interface is substantially increased, and the large majority of the metal atoms is in direct contact with the support. Noble metals are known to promote the support reduction leading to the formation of oxygen vacancies and partially reduced support cations [64,66,67]. This process could be accelerated in the case of subnanometer-sized metal particles and take place at much lower temperatures when compared to conventionally prepared catalysts with much larger particles. Therefore, it is possible that the reduction treatment in H_2 at 300 °C was sufficient to trigger the SMSI state in the highly dispersed dendrimer-derived Rh_{10}-G4OH/ZrO_2 and Rh_{20}-G4OH/ZrO_2 samples, which can in part explain the reduced chemisorptive properties for these samples.

In addition, the chemisorption results reported here for the dendrimer-derived Rh_{10}-G4OH/ZrO_2 and Rh_{20}-G4OH/ZrO_2 samples appear to be in agreement with similar results reported previously for well-defined Ir, Rh, and Pt clusters supported on various supports. For example, literature reports indicate that MgO-supported Ir clusters with nuclearity of four are characterized by a H/Ir value of 0.27 [68,69], while similar γ-Al_2O_3-supported Ir_4 clusters exhibit a H/Ir value of 0.13 [70]. Similarly, H/Rh values in the range of 0.10–0.16 were reported for Rh_6 clusters formed in cages of NaY and NaX zeolites [58], while a H/Pt ratio of approximately 0.01 was reported for Pt clusters in cages of NaY zeolite [71]. NaY-supported Rh, Pd, and Ru catalysts prepared from inorganic salts and incorporating metal clusters with sizes below 1 nm also show an unusual suppression of their propensity to adsorb hydrogen [72–74], suggesting that this phenomenon is not related to carbon deposits which could potentially be formed when organometallic compounds are used as precursors.

The common feature of the Rh_{10}-G4OH/ZrO_2 and Rh_{20}-G4OH/ZrO_2 samples and those listed above is the extremely small size of metal particles in the subnanometer range. It has been suggested previously that supported metal particles of this size are no longer metallic in character and the support must be regarded in these cases as a multidentate ligand [7]. It was further shown experimentally that the H/M ratio for supported Ir and Rh catalysts increases with increasing M–M first-shell coordination number

(and therefore, with metal particle size) and reaches the value of one when the size of the metal particles exceeds 1 nm [58,68].

Finally, based on the investigation of NaY- and HY-supported Ru catalysts incorporating Ru particles with average sizes in the range of 1–1.5 nm by a variety of different techniques, McCarthy et al. suggested that the metal-proton interactions are primarily responsible for the reduction of the hydrogen chemisorption with particle size [72]. This suggestion was further confirmed by computational studies of zeolite-supported six-atom clusters of Ru, Rh, Pd, Os, Ir, and Pt [75,76]. The results of these computational studies indicate that upon adsorption of M_6 clusters on hydroxylated surfaces of metal oxides or zeolites, these clusters are partially oxidized by surface OH groups and decorated by hydrogen. This process, known as a reverse hydrogen spillover, is strongly preferred energetically for most of the group 8 metals [75,76], suggesting that it is not possible to prepare supported clusters with metal surfaces that are clean and free of hydrogen impurities via a chemical route. The computational results further suggest that the reverse hydrogen spillover is maximized in the case of small metal clusters, while relatively large particles exhibit screening effects and their properties are approaching those of bulk metals. Based on these results, we can also propose that a partial decoration of the subnanometer-sized Rh particles in the Rh_{10}-G4OH/ZrO_2 and Rh_{20}-G4OH/ZrO_2 samples – as a result of reverse hydrogen spillover – may be another likely reason leading to the reduction of hydrogen chemisorption observed experimentally.

As indicated above, SMSI effects, loss of metallic character, and a reverse hydrogen spillover effect may be contributing to the reduced hydrogen chemisorption capacity of subnanometer supported metal particles, as documented experimentally in this and in previous studies. The relative importance of these mechanisms, which may be different for different catalysts, remains to be determined and is beyond the scope of this manuscript.

3.5. Catalytic hydrogenolysis of ethane

The hydrogenolysis of ethane to form methane is a classical structure-sensitive reaction used initially by Sinfelt and coworkers [45,77,78] to examine the effects of metal particle size on catalytic activity. Specifically, these authors reported an increase in specific catalytic activity with a decrease in metal particle size for supported platinum group metal catalysts. In the current study we have used the hydrogenolysis of ethane as a probe reaction to examine the surface structures of Rh particles in Rh/ZrO_2 samples prepared by different synthetic routes. The kinetic results obtained are summarized in Table 2.

Rh/ZrO_2 samples prepared by incipient wetness impregnation exhibit an increase in turnover frequency (TOF) with decreasing average Rh particle size over the 6.0–1.5 nm range. This result is consistent with the previous literature reports mentioned above [45,77–80]. Such an increase in specific catalytic activity with decreasing metal particle size for supported platinum group metal catalysts has been attributed to an increase in the fraction of low coordination highly energetic metal sites (i.e., corners and edges) adjacent to higher coordination planar sites [45,77–80]. It was further postulated that these low coordination sites facilitate C–C bond cleavage, while the high coordination sites represent adsorption sites for hydrogen atoms. Since it is generally assumed that the skeletal dehydrogenation of adsorbed ethane precedes the C–C bond rupture, both types of sites are needed in close proximity for the reaction to proceed at high rates.

This size dependence of the ethane hydrogenolysis TOF appears to be valid only for catalysts incorporating metal particles with average sizes of the order of 1.5 nm and above [45,77–80]. In contrast, supported catalysts with metal particle sizes below 1.5 nm show a different behavior for this reaction. For example, 1% Pt/γ-Al_2O_3 samples prepared by a sol–gel method and incorporating 1 nm particles were found to be one order of magnitude less active than similar samples with higher Pt loadings, and therefore, larger Pt particles [81]. Similarly, small Ru clusters located in the supercage of NaY and incorporating approximately 54 Ru atoms were found to be two orders of magnitude less active than larger Ru particles located on the external surface of the same zeolite [82]. When the number of Ru atoms per cluster decreased further from 54 to 25, the TOF also decreased by approximately a factor of two [82].

The kinetic results shown in Table 2 for the Rh/ZrO_2 samples examined in this study are also consistent with these reports. The TOF values decrease sharply as the average Rh particle size decreased below 1.5 nm, suggesting that this size is nearly optimal for the ethane hydrogenolysis reaction on Rh. Similarly, a maximum TOF value for ethane hydrogenolysis was observed for γ-Al_2O_3-supported Pt particles with a size of approximately 1.7 nm [83]. Furthermore, our results indicate that Rh particles with an average size of approximately 1.3 nm are less active by a factor of 50, while those with an average size of 0.8 nm were found to be less active by nearly three orders of magnitude (Table 2). Finally, the difference in TOF between 0.8 and 0.7 nm Rh particles was approximately a factor of two, which is similar to that observed in the case of Ru clusters with 25 and 54 metal atoms [82].

Apparent activation energy values calculated from the kinetic data for the subnanometer-sized Rh particles are approximately 29 kcal/mol, which is roughly 25% lower than the corresponding values for the catalysts incorporating larger Rh particles (Table 2). This observation is consistent with literature data reported previously for Pt/SiO_2 and indicating an increase in the apparent activation energy with an increase in metal particle size [79].

Based on the extended previous studies on ethane hydrogenolysis (e.g. [45,77–80]), it is reasonable to suggest that the kinetic data obtained in our work for highly dispersed Rh/ZrO_2 catalysts can be explained, at least in part, by a geometric effect. In advancing such an argument, one can suggest that subnanometer-sized metal particles in these samples are too small to have a sufficient number of sites available for the reaction to proceed smoothly. Isotopic transient kinetic analysis of ethane hydrogenolysis over Ru/SiO_2 catalysts modified with Cu indicated that 12 metal atoms is the minimum ensemble required for the hydrogenolysis of one ethane molecule [84]. Our EXAFS data indicate a Rh–Rh first-shell coordination number of 4.6 for the Rh_{20}-G4OH/ZrO_2 sample (Table 1) and suggest the formation of Rh nanoparticles incorporating no more than 20 metal atoms. Hence, it appears that with the family of ZrO_2-supported dendrimer-derived Rh catalysts we have nearly reached the critical Rh ensemble size required for the ethane hydrogenolysis reaction. These Rh ensembles may be capable of transforming ethane to methane at low rates, but certainly do not allow the reaction to proceed in a facile fashion due to the restricted number of contiguous Rh atoms available for an efficient accommodation of all reactants, intermediates, and reaction products.

Literature reports indicate that depending on the nature of the support, type of active metal, and experimental conditions, the hydrogenolysis of ethane can show a complex kinetic behavior which cannot be described by a single kinetic model [85,86]. However, the C–C bond cleavage step is considered in general to be the rate-determining step [87–90]. Results of DFT calculations [86,91] indicate that the activation energy of this step decreases with increasing degree of ethane dehydrogenation, suggesting that adsorbed ethylidyne and CHC species may be the most active intermediates for C–C bond scission [86,91]. In contrast, quantum chemical calculations indicate that regardless of the high abundance of ethylidyne intermediates the primary pathways for C–C bond cleavage proceed through highly hydrogenated activated

complexes such as $CHCH_3$ and C_2H_5 [92,93]. Despite these uncertainties regarding the mechanism of ethane hydrogenolysis, it is evident that the ethylidyne species formed under reaction conditions not only participate in site blocking [92,93], but can also induce structural changes in supported metal particles with sizes below 1 nm. For example, *in situ* EXAFS data reported for γ-Al_2O_3-supported Pt clusters incorporating approximately 25 metal atoms show that the value of $N_{Pt\text{-}Pt}$ decreased from 6.5 to 3.0 when ethylidyne species were formed on the Pt surface [94]. Since the ethylidyne species are known for restructuring of Pt(1 1 1) and Rh(1 1 1) surfaces [95,96], such substantial changes observed in the first-shell Pt–Pt coordination number in the case of small Pt clusters can be related not only to changes in their morphology (i.e., shape), as was suggested previously [94], but also to their partial fragmentation. The presence of ethylidyne species on the surface of the subnanometer-sized Rh particles in the Rh_{10}-G4OH/ZrO_2 and Rh_{20}-G4OH/ZrO_2 samples under ethane hydrogenolysis conditions could also trigger structural changes similar to those observed in the case of Pt clusters, leading to the formation of even smaller metal ensembles. Such ensembles would not be capable of accommodating both the hydrogen atoms formed during the dehydrogenation of adsorbed ethane and the dehydrogenated C_2H_x ($x < 6$) species, resulting in very low TOFs. Additional *in situ* EXAFS work is needed to further examine this hypothesis.

Finally, many kinetic models consider both the skeletal dehydrogenation of adsorbed ethane species and the hydrogenation of methyl intermediates as relatively quick steps in the mechanism of ethane hydrogenolysis. To proceed efficiently, the first requires the accommodation of hydrogen atoms striped off the C_2H_x intermediates, while the second requires an abundance of hydrogen atoms in the vicinity of the CH_x intermediates formed. Since our data clearly indicate that the hydrogen chemisorption on Rh is reduced substantially in the case of the subnanometer-sized Rh particles, we expect that the rates of these steps will also be affected beyond the geometric effects discussed in the previous paragraphs. Whether a decrease of these rates will be significant enough to affect the overall rate of the reaction is not clear at this point.

Overall, the low TOF values observed for ethane hydrogenolysis in the case of subnanometer-sized Rh particles can be reasonably justified by several factors as discussed above. Additional work is needed before we can determine the relevant importance of these factors. However, the data reported here provide unambiguous evidence that the properties of supported Rh particles with sizes below a certain threshold are significantly different from those of larger metal particles formed in conventionally prepared samples.

4. Conclusions

We have demonstrated that nearly uniform sub-nanometer Rh particles can be prepared on a ZrO_2 support via the dendrimer-mediated synthetic route. EXAFS characterization of each step involved in this process indicates that Rh_3 clusters are formed within the dendrimer interior structure in aqueous solutions and the resulting Rh-dendrimer nanocomposites can be deposited onto a high surface area ZrO_2 support. Subsequent thermal treatments in O_2 and H_2 are required to remove the dendrimer component and to form stable Rh nanoparticles. Very limited sintering of Rh was observed during these thermal treatments, leading to the formation of Rh particles with sub-nanometer dimensions. The catalytic properties of these materials for ethane hydrogenolysis are substantially different from those of larger Rh particles. Our results represent a breakthrough in the synthesis of uniform and highly dispersed supported Rh catalysts and open up promising opportunities for the preparation of additional catalysts with more complex chemical compositions.

Acknowledgments

The authors acknowledge the financial support of Toyota Motor Engineering and Manufacturing Inc. (USA) and Toyota Motor Corporation (Japan). A part of this research was carried out at the Stanford Synchrotron Radiation Laboratory, a national user facility operated by Stanford University on behalf of the US Department of Energy, Office of Basic Energy Sciences. The assistance of the beam line staff at SSRL is gratefully acknowledged. Finally, the authors acknowledge Dongxia Liu for collecting some of the HRTEM images, Yaritza Lopez-De Jesus and Zahra Nazarpoor for their assistance with some of the TPO and H_2 chemisorption measurements, and Larry Allard and staff at Oak Ridge National Laboratory for access to HRTEM.

References

[1] A. König, G. Herding, B. Hupfeld, Th. Richter, K. Weidmann, Top. Catal. 16/17 (2001) 23.
[2] G.J. Antos, A.M. Aitani (Eds.), Catalytic Naphtha Reforming, Dekker, New York, 2004.
[3] A.K. Shukla, R.K. Raman, Ann. Rev. Mater. Res. 33 (2003) 155.
[4] M. Boudart, J. Mol. Catal. 30 (1985) 27.
[5] B.C. Gates, J. Mol. Catal. A 163 (2000) 55.
[6] A. Siani, O.S. Alexeev, B. Captain, G. Lafaye, P. Marécot, R.D. Adams, M.D. Amiridis, J. Catal. 255 (2008) 162.
[7] Z. Xu, F.-S. Xiao, S.K. Purnell, O. Alexeev, S. Kawi, S.E. Deutsch, B.C. Gates, Nature (London) 372 (1994) 346.
[8] Y. Xu, W.A. Shelton, W.F. Schneider, J. Phys. Chem. A 110 (2006) 5839.
[9] U. Heiz, W.-D. Schneider, J. Phys. D: Appl. Phys. 33 (2000) R85.
[10] L.M. Molina, J.A. Alfonso, J. Phys. Chem. C 111 (2007) 6668.
[11] R. Van Hardeveld, F. Hartog, Surf. Sci. 15 (1969) 189.
[12] U. Heiz, A. Sanchez, S. Abbet, W.-D. Schneider, J. Am. Chem. Soc. 121 (1999) 3214.
[13] B. Kalita, R.C. Deka, J. Chem. Phys. 127 (2007) 244306.
[14] P. Braunstein, L.A. Oro, P.R. Raithby, Metal Clusters in Chemistry: Molecular Metal Clusters, Wiley, Weinheim, 1999.
[15] G. Ertl, H. Knözinger, J. Weitkamp (Eds.), Handbook of Heterogeneous Catalysis, VCH, Weinheim, 1997.
[16] C.P. Vinod, G.U. Kulkarni, C.N.R. Rao, Chem. Phys. Lett. 289 (1998) 329.
[17] B.C. Gates, Top. Catal. 14 (2001) 173.
[18] O.S. Alexeev, B.C. Gates, Ind. Eng. Chem. Res. 42 (2003) 1571.
[19] D. Astruc, Nanoparticles and Catalysis, Wiley-VCH, Weinheim, 2008.
[20] A. Roucoux, J. Schulz, H. Patin, Chem. Rev. 102 (2002) 3757.
[21] C. Burda, X. Chen, R. Narayanan, M.A. El-Sayed, Chem. Rev. 105 (2005) 1025.
[22] B.L. Cushing, V.L. Kolesnichenko, C.J. O'Connor, Chem. Rev. 104 (2005) 3893.
[23] R. Andrés, E. de Jesús, J.C. Flores, New J. Chem. 31 (2007) 1161.
[24] H. Lang, R.A. May, B.L. Iversen, B.D. Chandler, J. Am. Chem. Soc. 125 (2003) 14832.
[25] R.W.J. Scott, O.M. Wilson, R.M. Crooks, Chem. Mater. 16 (2004) 5682.
[26] R.W.J. Scott, C. Sivadinarayana, O.M. Wilson, Z. Yan, D.W. Goodman, R.M. Crooks, J. Am. Chem. Soc. 127 (2005) 1380.
[27] G. Lafaye, A. Siani, P. Marecot, M.D. Amiridis, C.T. Williams, J. Phys. Chem. B 110 (2006) 7725.
[28] R.W.J. Scott, O.M. Wilson, R.M. Crooks, J. Phys. Chem. B 109 (2005) 692.
[29] R.M. Crooks, M. Zhao, L. Sun, V. Chechik, L.K. Yeung, Acc. Chem. Res. 34 (2001) 181.
[30] O.S. Alexeev, A. Siani, G. Lafaye, C.T. Williams, H.J. Ploehn, M.D. Amiridis, J. Phys. Chem. B 110 (2006) 24903.
[31] D.S. Deutsch, C.T. Williams, M.D. Amiridis, in: J. Regalbuto (Ed.), Catalyst Preparation: Science and Engineering, CRC Press, 2006.
[32] S.Y. Chin, O.S. Alexeev, M.D. Amiridis, J. Catal. 243 (2006) 329.
[33] A.P. Gloor, R. Prins, J. Phys. Chem. 98 (1994) 9865.
[34] M. Vaarkamp, J.C. Linders, D.C. Koningsberger, Physica B 208–209 (1995) 159.
[35] D.C. Koningsberger, in: C. A Melendres, A. Tadjeddine (Eds.), Synchrotron Techniques in Interfacial Electrochemistry, Kluwer, Dordrecht, 1994, p. 181.
[36] E.A. Stern, Phys. Rev. B 48 (1993) 9825.
[37] E.O. Brigham, The Fast Fourier Transform, Prentice-Hall, Englewood Cliffs, NJ, 1974.
[38] M. Tromp, J.A. van Bokhoven, A.M. Arink, J.H. Bitter, G. van Koten, D.C. Koningsberger, Chem. Eur. J. 8 (2002) 5667.
[39] P.S. Kirlin, F.B.M. van Zon, D.C. Koningsberger, B.C. Gates, J. Phys. Chem. 94 (1990) 8439.
[40] J.B.A.D. van Zon, D.C. Koningsberger, H.F.J. van't Blik, D.E. Sayers, J. Chem. Phys. 82 (1985) 5742.
[41] M. Vaarkamp, Ph.D. Thesis, Eindhoven University, The Netherlands, 1993.
[42] F.W. Lytle, D.E. Sayers, E.A. Stern, Physica B 158 (1988) 701.
[43] D.C. Koningsberger, B.L. Mojet, G.E. van Dorssen, D.E. Ramaker, Top. Catal. 10 (2000) 143.
[44] J.E. Benson, M. Boudart, J. Catal. 4 (1965) 704.
[45] J.H. Sinfelt, D.J.C. Yates, J. Catal. 8 (1967) 82.

[46] R.W.G. Wyckoff, Crystal Structures v.2, Wiley, New York, 1967.
[47] H. Baerighausen, B.K. Handa, J. Less-Common Met. 6 (1964) 226.
[48] D.A. Palmer, G.M. Harris, Inorg. Chem. 14 (1975) 1316.
[49] K. Kuno, J. Ito, Nippon Kagaku Kaishi 6 (1995) 432.
[50] A.V. Belyaev, M.A. Fedotov, V.I. Korsunskii, A.B. Venediktov, S.P. Khranenko, Koordinatsionnaya Khimiya 10 (1984) 911.
[51] D.C. Koningsberger, R. Prins, X-ray Absorption. Principles, Applications, Techniques of EXAFS, SEXAFS and XANES, Wiley, New York, 1988.
[52] D.A. Tomalia, A.M. Naylor, W.A. Goddard, Angew. Chem. Int. Ed. Engl. 29 (1990) 138.
[53] D. Liu, J. Gao, C.J. Murphy, C.T. Williams, J. Phys. Chem. B 108 (2004) 12911.
[54] P.K. Maiti, T. Cagin, S.T. Lin, W.A. Goddard, Macromolecules 38 (2005) 979.
[55] Y.L. Gu, H. Xie, J.X. Gao, D.X. Liu, C.T. Williams, C.J. Murphy, H.J. Ploehn, Langmuir 21 (2005) 3122.
[56] D.S. Deutsch, G. Lafaye, D.X. Liu, B. Chandler, C.T. Williams, M.D. Amiridis, Catal. Lett. 97 (2004) 139.
[57] D.S. Deutsch, A. Siani, P.T. Fanson, H. Hirata, S. Matsumoto, C.T. Williams, M.D. Amiridis, J. Phys. Chem. C. 111 (2007) 4246.
[58] W.A. Weber, B.C. Gates, J. Catal. 180 (1998) 207.
[59] F.S. Lai, B.C. Gates, Nano Lett. 1 (2001) 583.
[60] W.A. Weber, B.C. Gates, J. Phys. Chem. B. 101 (1997) 10423.
[61] B.J. Kip, F.B.M. Duivenvoorden, D.C. Koningsberger, R. Prins, J. Catal. 105 (1987) 26.
[62] S.J. Tauster, S.C. Fung, R.L. Garten, J. Am. Chem. Soc. 100 (1978) 170.
[63] M.A. Vannice, R.L. Garten, J. Catal. 56 (1979) 236.
[64] F. Pesty, H.-P. Steinruck, T.E. Madey, Surf. Sci. 339 (1995) 83.
[65] D.R. Mullins, K.Z. Zhang, Surf. Sci. 513 (2002) 163.
[66] R.T.K. Baker, S.J. Tauster, J.A. Dumesic (Eds.), Strong Metal Support Interactions, American Chemical Society, Washington, D.C., 1986.
[67] T. Huizinga, R. Prins, J. Phys. Chem. 85 (1981) 2156.
[68] O.S. Alexeev, D.-W. Kim, B.C. Gates, J. Mol. Catal. A 162 (2000) 67.
[69] F.-S. Xiao, Z. Xu, O. Alexeev, B.C. Gates, J. Phys. Chem. 99 (1995) 1548.
[70] O. Alexeev, G. Panjabi, B.C. Gates, J. Catal. 173 (1998) 196.
[71] T. Kubo, H. Arai, H. Tominaga, T. Kunugi, Bull. Chem. Soc. Jpn. 45 (1972) 607.
[72] T.J. McCarthy, C.M.P. Marques, H. Trevino, W.M.H. Sachtler, Catal. Lett. 43 (1997) 11.
[73] L. Xu, Z. Zhang, W.M.H. Sachtler, J. Chem. Soc. Faraday Trans. 88 (1992) 2291.
[74] D.C. Tomczak, G.-D. Lei, V. Schunemann, H. Trevino, W.M.H. Sachtler, Microporous Mater. 5 (1996) 263.
[75] G.N. Vayssilov, N. Rosch, Phys. Chem. Chem. Phys. 7 (2005) 4019.
[76] G.N. Vayssilov, B.C. Gates, N. Rosch, Angew. Chem. Int. Ed. 42 (2003) 1391.
[77] D.J.C. Yates, J.H. Sinfelt, J. Catal. 8 (1967) 348.
[78] J.H. Sinfelt, Catal. Rev. 3 (1970) 175.
[79] H. Song, R.M. Rioux, J.D. Hoefelmeyer, R. Komor, K. Niesz, M. Grass, P. Yang, G.A. Somorjai, J. Am. Chem. Soc. 128 (2006) 3027.
[80] R.M. Rioux, H. Song, J.D. Hoefelmeyer, P. Yang, G.A. Somorjai, J. Phys. Chem. B 109 (2005) 2192.
[81] I.H. Cho, S.B. Park, S.J. Cho, R. Ryoo, J. Catal. 173 (1998) 295.
[82] I.H. Cho, S.J. Cho, S.B. Park, R. Ryoo, J. Catal. 153 (1995) 232.
[83] D. Nazimek, J. Ryczkowski, React. Kinet. Catal. Lett. 40 (1989) 145.
[84] B. Chen, J.G. Goodwin, J. Catal. 158 (1996) 228.
[85] G.A. Martin, R. Dutartre, S. Yuan, C. Marquez-Alvarez, C. Mirodatos, J. Catal. 177 (1998) 105.
[86] A.V. Zeigarnik, R.E. Valdes-Perez, O.N. Myatkovskaya, J. Phys. Chem. B 104 (2000) 10578.
[87] B. Chen, J.G. Goodwin, J. Catal. 154 (1995) 1.
[88] S.B. Shang, C.N. Kenney, J. Catal. 134 (1992) 134.
[89] F. Zaera, G.A. Somorjai, J. Phys. Chem. 89 (1985) 3211.
[90] M.W. Smale, T.S. King, J. Catal. 129 (1990) 335.
[91] A.V. Zeigarnik, O.N. Myatkovskaya, Kinet. Catal. 42 (2001) 418.
[92] R.D. Cortright, R.M. Watwe, B.E. Spiewak, J.A. Dumesic, Catal. Today 53 (1999) 395.
[93] R.D. Cortright, R.M. Watwe, J.A. Dumesic, J. Mol. Catal. A 163 (2000) 91.
[94] O.S. Alexeev, F. Li, M.D. Amiridis, B.C. Gates, J. Phys. Chem. B 109 (2005) 2338.
[95] M.A. Van Hove, G.A. Somorjai, J. Mol. Catal. A 131 (1998) 243.
[96] Q. Ge, D.A. King, J. Chem. Phys. 110 (1999) 4699.